An in situ and ex situ study of χ phase formation in a hypoeutectic Fe-based hardfacing alloy

Author(s):
Wieczerzak, Krzysztof; Michler, Johann; Wheeler, Jeffrey M.; Lech, Sebastian; Chulist, Robert; Gondek, Łukasz; Czub, Joanna; Hoser, Andreas; Schell, Norbert; Bała, Piotr

Publication date:
2020-03

Permanent link:
https://doi.org/10.3929/ethz-b-000387266

Originally published in:
Materials & Design 188, https://doi.org/10.1016/j.matdes.2019.108438

Materials and Design 188 (2020) 108438

Contents lists available at ScienceDirect

Materials and Design

journal homepage: www.elsevier.com/locate/matdes

An in situ and ex situ study of χ phase formation in a hypoeutectic Fe-based hardfacing alloy

K. Wieczerzak [a,b,*], J. Michler [a], J.M. Wheeler [c], S. Lech [b,d], R. Chulist [e], Ł. Gondek [f], J. Czub [f], A. Hoser [g], N. Schell [h], P. Bała [b,i]

[a] Empa, Swiss Federal Laboratories for Materials Testing and Research, Laboratory for Mechanics of Materials and Nanostructures, Feuerwerkerstrasse 39, Thun CH-3602, Switzerland
[b] AGH University of Science and Technology, Faculty of Metals Engineering and Industrial Computer Science, Al. A. Mickiewicza 30, 30-059 Krakow, Poland
[c] ETH Zurich, Department of Materials, Laboratory for Nanometallurgy, Vladimir-Prelog-Weg 5, Zürich 8093, Switzerland
[d] AGH University of Science and Technology, International Centre of Electron Microscopy for Materials Science and Faculty of Metals Engineering and Industrial Computer Science, Al. A. Mickiewicza 30, 30-059 Krakow, Poland
[e] Institute of Metallurgy and Materials Science, Polish Academy of Sciences, Reymonta St. 25, 30-059 Kraków, Poland
[f] AGH University of Science and Technology, Faculty of Physics and Applied Computer Science, Al. A. Mickiewicza 30, 30-059 Krakow, Poland
[g] Helmholtz-Zentrum Berlin, Hahn-Meitner-Platz 1, 14109 Berlin, Germany
[h] Institute of Materials Research, Helmholtz-Zentrum Geesthacht, Max-Planck-Strasse 1, D-21502 Geesthacht, Germany
[i] AGH University of Science and Technology, Academic Centre for Materials and Nanotechnology, Al. A. Mickiewicza 30, 30-059 Krakow, Poland

HIGHLIGHTS

- Formation of the χ phase in the Fe-25Cr-7Mo-0.8C alloy was established.
- Phase and microstructural evolution of the alloy was determined.
- Annealing temperature has a significant effect on the χ phase morphology.
- Annealing temperature affects the χ phase nucleation sites.
- The χ phase is beneficial for hardness and wear resistance enhancement.

GRAPHICAL ABSTRACT

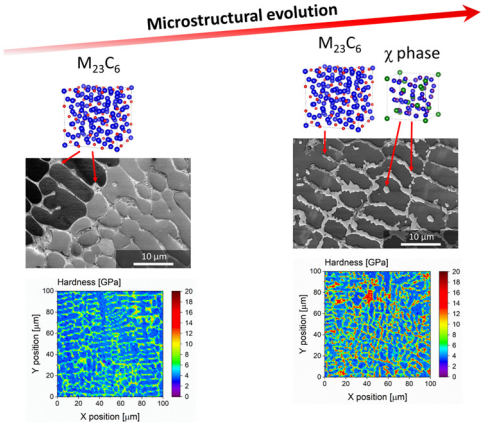

ARTICLE INFO

Article history:
Received 28 August 2019
Received in revised form 12 November 2019
Accepted 16 December 2019
Available online 17 December 2019

Keywords:
Hypoeutectic alloy

ABSTRACT

In this work, the effect of topologically close-packed χ phase on the microstructure and properties of the rapidly solidified hypoeutectic iron-based Fe-25Cr-7Mo-0.8C alloy was investigated. The novelty of the work is based on the introduction of χ phase into the Fe-based hypoeutectic alloy with the aim of reducing the mean free path of the matrix and increasing abrasive resistance. The phase composition was studied using in situ neutron and ex situ X-ray synchrotron diffraction. The microstructural evolution was analyzed via scanning and transmission electron microscopy and modelled using CALPHAD thermodynamic calculations. The mechanical behavior of the evolving microstructure was quantified using high-speed nanoindentation mapping. At low temperatures

* Corresponding author at: Empa, Swiss Federal Laboratories for Materials Testing and Research, Laboratory for Mechanics of Materials and Nanostructures, Feuerwerkerstrasse 39, Thun CH-3602, Switzerland.
E-mail address: krzysztof.wieczerzak@empa.ch (K. Wieczerzak).

https://doi.org/10.1016/j.matdes.2019.108438

Fe-Cr-Mo-C system
Hardfacing
$M_{23}C_6$ carbides
TCP phase
Wear

(650 °C), the χ phase nucleates mainly in dendrite areas and exhibits a needle-like morphology caused by high misfit with the ferritic matrix. At higher temperatures (800 °C), the χ phase nucleates on carbide/matrix interfaces and in dendrites and is characterized by a blocky morphology. Simultaneously, the evolution of $M_{23}C_6$ carbide morphology towards a continuous and solid network of precipitates was observed. Such changes in the alloy's microstructure induced an increase in hardness of about 16% and resulted in the reduction of the average scratch depth in comparison to as-cast state.

1. Introduction

Hardfacing is a process in which an alloy with superior properties (e.g. hardness, tribological wear resistance and corrosion resistance) is deposited onto a substrate or worn surface to increase their performance and, consequently, operational lifetime. Hardfacing alloys working at elevated temperatures are typically heterogeneous materials and their performance depends on the properties of the constituent phases. Such alloys dedicated to high-temperature applications contain a tough matrix and are typically strengthened by hard phases, such as carbides, borides or topologically close-packed (TCP) phases, also referred to as Frank-Kasper (FK) phases [1–3]. These phases exhibit high thermodynamic stability and are embedded mainly in high alloyed iron-, nickel- or cobalt-based matrices [4]. To sustain long-term operation, the microstructure of the hardfacing alloy should be stable in terms of phase composition and morphology of each phase over time [5]. Hardfacing alloys can be deposited via conventional spraying or arc welding methods, as wells as via sophisticated laser-based and additive manufacturing-based approaches [2,4,6,7]. The major difference between the previously mentioned deposition techniques is the amount of heat input, which affects the thermal gradient and solidification conditions of the deposited material. Consequently, the microstructure and properties of such materials are strongly dependent on deposition parameters and technique. The properties of hardfacing alloys in many cases can be enhanced through heat treatment, which causes changes in phase composition and/or morphology of the strengthening phases [8–10]. In terms of alloys dedicated for high-temperature applications, long exposure to elevated temperatures can also induce changes in their properties [11]. To determine the potential and limitations of commercial or newly designed hardfacing alloys, it is, therefore, necessary to understand the effect of temperature on their phase composition and the morphology of the strengthening phases.

This paper focuses on the microstructural and phase evolution in the rapidly solidified hypoeutectic Fe-25Cr-7Mo-0.8C alloy with a ferritic matrix. Within this work, emphasis was placed on the investigation of the χ phase formation in the above-mentioned alloy and its effect on the microstructure and properties. The selected alloy is strengthened by eutectic, chromium-rich carbides and contains a high amount of χ phase formers, namely chromium and molybdenum. It was designed by following the previously reported concept of hypoeutectic iron-based alloys, additionally strengthened by TCP phases [12]. The χ phase with a $I\bar{4}3m$ space group and 58 atoms in the unit cell belongs to the TCP phase family [13]. It exhibits relatively high hardness at room and at elevated temperature, similarly to chromium-rich carbides [14]. For instance, Westbrook [14] reported the hardness of the χ phase from the Fe-Cr-Mo system at room temperature (RT) and at 800 °C, equal to 1000 and 440 HV, respectively. Gwalani et al. [15], who investigated the Al-Ti-Co-Cr-Fe-Ni high entropy alloy, found the χ phase as the matrix of the alloy with a measured hardness at room temperature of 1090 HV, similar to the value reported by Westbrook [14]. Therefore, it seems that the χ phase is a promising candidate to enhance hot hardness. Furthermore, if it is precipitated in a controlled manner, it should reduce the free path of the matrix, thus most probably increasing tribological properties, especially abrasive wear resistance at elevated temperatures [12,16].

The alloy from the Fe-Cr-Mo-C system selected for this study was designed to exhibit good corrosion, oxidation and tribological wear resistance [12]. Good physicochemical properties in Fe-based hardfacing alloys can be achieved through the addition of chromium, typically in the range between 10.5 and 30% (all compositions in this work except Table 2 are given in wt%) that allows for the formation of a protective passive film on the surface. The addition of molybdenum can enhance localized corrosion resistance, particularly in acidic conditions, and simultaneously increase the tendency for TCP phase precipitation [17–19]. The addition of carbon into the Fe-Cr-Mo system enables the precipitation of eutectic carbides [20]. As carbides and TCP phases exhibit high hardness, they should enhance the alloy's wear resistance if their volume fraction and morphology are properly designed [21,22]. TCP phases are mostly undesirable in metallic materials, such as nickel-based superalloys, cobalt-based alloys and most stainless steels, as they deteriorate the mechanical (e.g. toughness) and physicochemical (e.g. corrosion resistance) properties [23–26]. Nevertheless, in the case of hardfacing alloys containing a significant volume fraction of hard phases, the toughness is naturally reduced in comparison to single-phase alloys with a comparable chemical composition of the matrix [27]. In terms of corrosion resistance, precipitation of hard primary or secondary phases causes a depletion of the matrix in alloying elements (Cr, Mo, etc.) that are important from the corrosion resistance point of view. After solidification, such depleted regions can be found in the vicinity of strengthening phases containing high amount of alloying elements [28]. Therefore, when designing the chemical composition of the alloy, the aforementioned phenomena were taken into account.

2. Experimental

2.1. Material synthesis

The selection of the Fe-25Cr-7Mo-0.8C alloy for investigation was made using previously reported thermodynamic calculations [12]. The alloy was synthesized using arc melting and suction casting. The suction casting technique allows obtaining solidification conditions, similar to those observed in arc welding processes. Furthermore, the major advantage of the suction casting technique is the lack of substrate and dilution effect, which facilitates microstructure analysis. The synthesis procedure was analogous to that of [29]. The alloy composition was determined using the Foundry-Master (WAS) optical emission spectrometer. The results are summarized in Table 1.

2.2. Phase composition simulations

To predict the equilibrium phase composition of the Fe-25Cr-7Mo-0.8C alloy, thermodynamic calculations were carried out using ThermoCalc software [30] with the database for Fe-alloys TCFE7. Fig. 1

Table 1
Chemical composition of the investigated alloy (wt%).

Cr	Mo	C	Si	Mn	P	S	Fe
24.9	6.8	0.815	0.203	0.121	0.016	0.023	Bal.

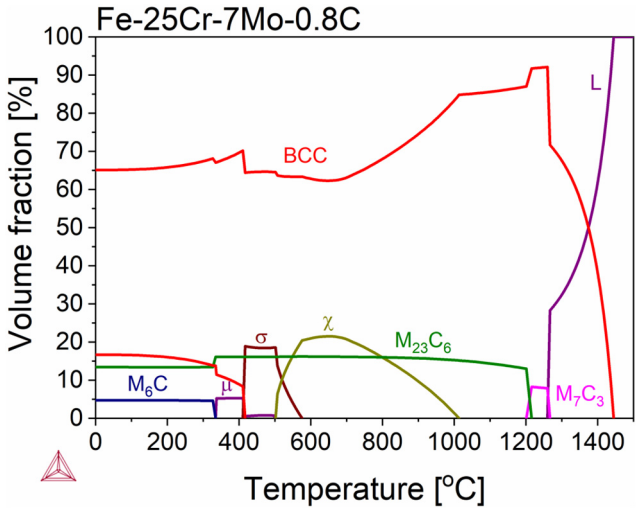

Fig. 1. Phase volume fraction vs temperature simulations for the Fe-25Cr-7Mo-0.8C alloy.

presents results of thermodynamic simulations of the volume fraction of equilibrium phases vs temperature for the investigated alloy. The phase composition of the alloy lies outside the face-centered cubic (FCC) austenite field, which is influenced by the high contents of ferrite stabilizers: chromium and molybdenum. Consequently, body-centered cubic (BCC) ferrite is the only solid solution phase that is stable up to the liquidus temperature. The occurrence of the $L \rightarrow \alpha + M_7C_3$ eutectic reaction can be observed. Subsequently, the M_7C_3 carbide undergoes transformation into $M_{23}C_6$ in solid phase. It is predicted that with decreasing temperature, the precipitation of TCP phases from the ferritic matrix, such as the χ phase, σ phase and μ phase, will occur. Below 330 °C, the partial transformation of $M_{23}C_6$ into M_6C takes place.

2.3. Phase analysis

2.3.1. High temperature in situ neutron diffraction

The phase composition analysis of the alloy at selected temperatures was performed using neutron diffraction studies carried out at the BERII Research Reactor in Helmholtz-Zentrum Berlin using the E6 diffractometer. The incident neutron wavelength was 2.421 Å. The powder produced via milling of the suction-cast rod was used for the experiment. The milling was carried out in wet mode using ethanol in a commercial Mixer Mill MM 400 from Retsch. The sample was placed in an amorphous quartz tube, which was purified (evacuated and flushed with Ar) and finally filled with high purity Ar (6 N) at 0.2 bar of overpressure (the overpressure was kept constant during the entire experiment). The tube containing the sample was installed in a high-temperature furnace. Prior to the experiment, calibration measurements were performed using Y_2O_3 (20 °C) and an empty quartz tube (200–1250 °C) to estimate profile parameters and the sample environment contributions to the diffraction patterns. The diffraction patterns were collected at a step of 50 °C and a 10 °C/min ramp was used to reach the required temperature, which was next held for 15 min for temperature stabilization. The measurement time for each temperature was 2 h.

2.3.2. Ex situ X-ray diffraction

The phase composition analysis of the alloy in as-cast state and after heat treatment was performed using high energy synchrotron X-ray radiation. Samples were prepared from the suction cast rod with the dimensions of 10 (height) × 3 (diameter) mm. Heat treatment was performed on three samples under a high purity argon atmosphere in the Linseis L78 RITA dilatometer. The samples were heated with a rate of 5 °C/s up to 650, 800 and 1000 °C, respectively, then annealed at the selected temperatures for 4 h, followed by rapid cooling at the rate of 100 °C/s until reaching room temperature. XRD measurements were carried out using the HZG beamline (P07B) located at PETRA III (electro storage ring operating at an energy of 6 GeV with beam current equal 100 mA) at DESY, Hamburg, Germany. During the experiment, high-energy synchrotron radiation with a wavelength of 0.153495 Å was applied. The obtained 2D patterns were integrated using Fit2D software and presented in a graph of relative intensity as a function of 2Θ angle. To eliminate the effect of crystallographic texture, the samples were continuously rotated 180 degrees around the ω-axis during the measurement [31]. Such an approach allowed collecting all diffraction reflections onto one image. To determine lattice parameters of the identified phases, the XRD data, similarly as neutron diffraction data, were analyzed using the profile-fitting software TOPAS 5 [32], based on the Rietveld method [33].

2.4. Microstructure investigations

Microstructural observations were carried out using the FEI VERSA 3D scanning electron microscope (SEM), equipped with an Apollo XP SDD energy dispersive spectroscopy (EDX) detector. Experiments were performed on the same samples as for ex situ XRD experiments. Analysis was performed on polished samples, as well as after selective electrolytic etching in the A2 solution provided by Struers. EDX analysis was performed using an accelerating voltage of 15 kV. Quantitative chemical analysis was carried out using the ZAF correction.

The transmission electron microscopy (TEM) studies were performed on TEM lamellae, prepared via focused ion-milling (FIB technique) using the FEI QUANTA 3D 200i system. The TEM experiment was conducted using the FEI TECNAI TF 20 X-TWIN electron microscope, equipped with a field emission electron gun (FEG), operated at 200 kV.

2.5. Vickers hardness and nanoindentation analysis

Vickers hardness tests were performed on polished samples using the TUKON 2500 hardness tester by Wilson Hardness. Testing was carried out with a 9.8 N load (HV1) and a 10 s indentation time with a minimum of five measurements on each specimen.

Nanoindentation mapping was performed using the NanoBlitz module on an iNano nanoindenter (Nanomechanics, Inc., Oak Ridge, USA). An indentation array of 200 × 200 indents (total 40,000) was made on each sample. Indentations were spaced at an interval of 1 μm to ensure the suggested indentation depth/spacing ratio of 10 was maintained [34] for the applied load of 1 mN. Tests were performed at room temperature using a Berkovich diamond indenter.

2.6. Scratch tests

Scratch tests were carried out to determine the effect of the χ phase on the fundamental interaction between a sliding abrasive particle (spheroconical diamond indenter of 10 μm radius) and the surface of the investigated iron-based alloy [35]. The experiment was performed using the MTS Nano Indenter XP. Five 500 μm long scratches were made on each sample using increasing load from 0 to 500 mN. The velocity used to perform the test scratch cycle was 50 μm/s. The morphology of scratches was analyzed via the Sensofar 3D optical Profilometer in confocal mode. Displacement into surface (scratch depth) results were corrected by the specimens' topographic profile.

3. Results and discussion

3.1. In situ measurements of phase evolution vs temperature

High-temperature neutron diffraction patterns are presented in Fig. 2. The studies reveal that at low temperatures, only ferrite (BCC solid solution) and $M_{23}C_6$ carbides are present in the investigated alloy, in agreement with thermodynamic simulations in Section 2.2. However, the formation of the σ phase, predicted in abovementioned

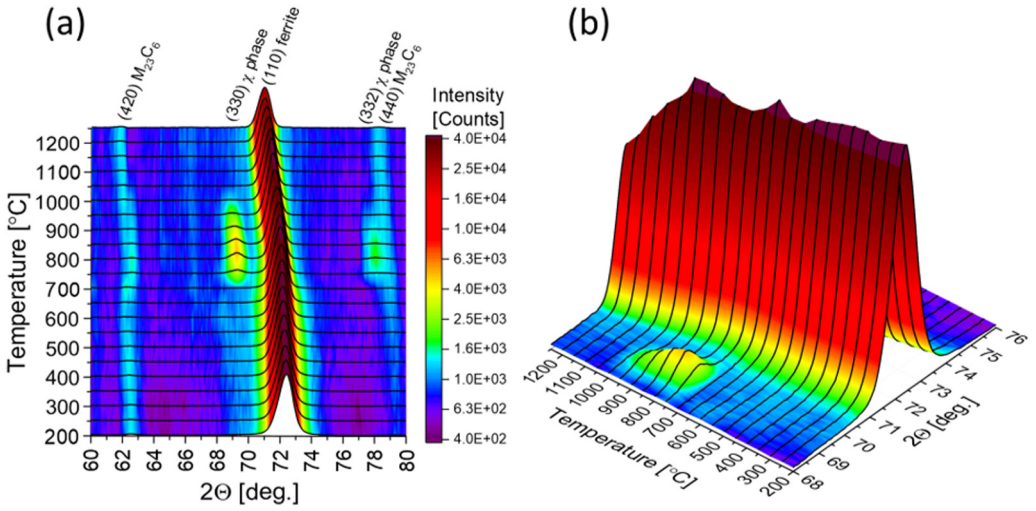

Fig. 2. (a) Neutron powder diffraction patterns collected in situ at high temperatures for the Fe-25Cr-7Mo-0.8C alloy. (b) Enlarged range of the main reflections group. The map of main reflection intensities and position change vs temperature was plotted based on 22 measurements, collected at a step of 50 °C in the temperature range 200–1250 °C.

calculations, was not observed. As the chemical composition of the σ phase is significantly different than ferrite or $M_{23}C_6$ carbides, its precipitation requires diffusion of substitutional elements between phases. The occurrence of the σ phase is predicted at lower temperatures compared to the χ phase (Fig. 1). It is well known that the diffusion of elements slows down as the temperature decreases, therefore the absence of the σ phase is most likely related to its precipitation kinetics.

It can be seen that up to 700 °C, both ferrite and $M_{23}C_6$ carbides are stable. However, starting from 700 °C, additional reflections associated with the χ phase rapidly appear. In Fig. 2b, one can notice that the intensity of the (330) reflection of the χ phase reaches its highest intensity at 800 °C. The χ phase formation is related with some anomalous behavior of the reflections of $M_{23}C_6$ carbides. For instance, the (420) reflection suddenly moves towards higher 2θ angles, while during dissolution of the χ phase, it goes back to expected position (Fig. 2a). The (420) reflection position change above the $M_{23}C_6$ carbide indicates a decrease in the lattice parameter of this phase (Fig. 2a). Although the (420) reflection is relatively weak, it is possible to spot a splitting of the reflection above 850 °C. This is related to changes in metal stoichiometry in the carbide during the χ phase dissolution. On the other

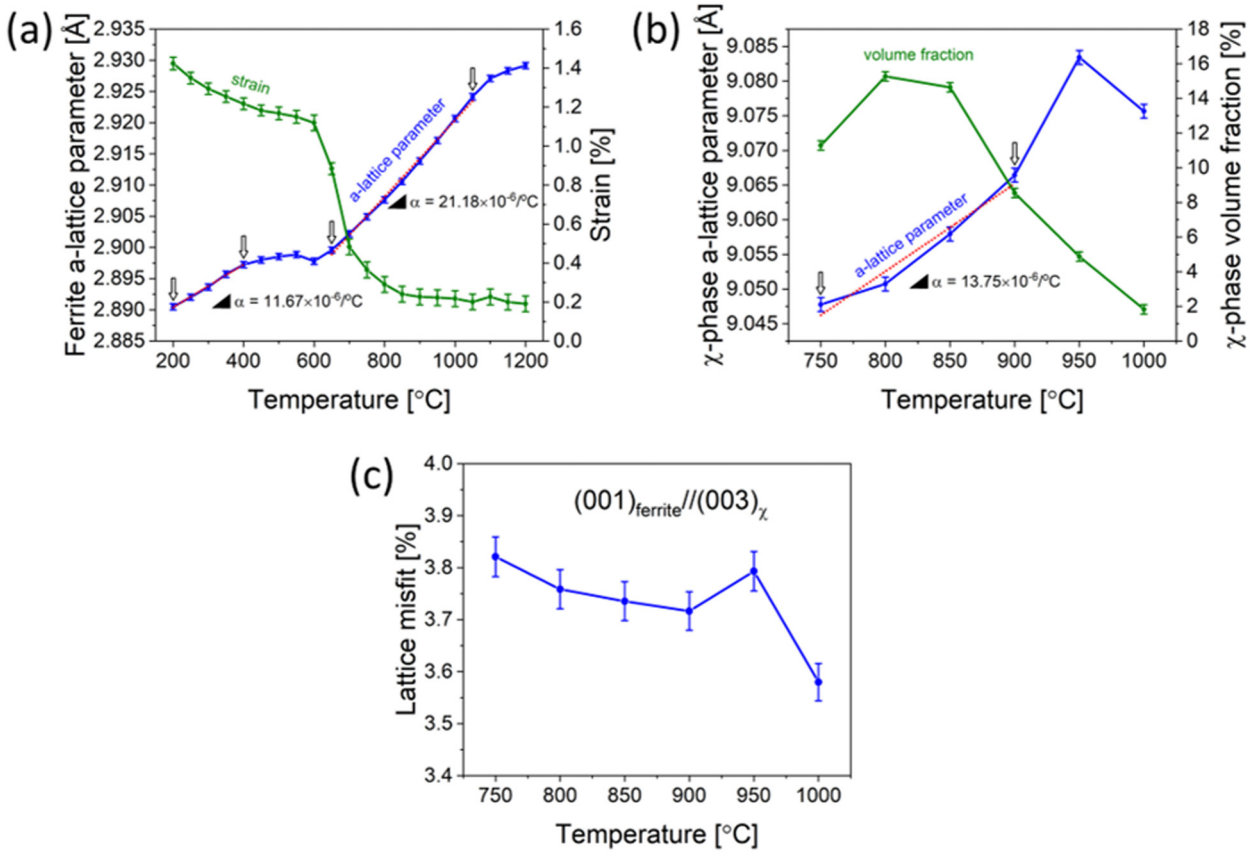

Fig. 3. Quantitative neutron powder diffraction analysis for the Fe-25Cr-7Mo-0.8C alloy. (a) Lattice parameter and strain for ferrite vs temperature. (b) Lattice parameter and volume fraction for the χ phase in the Fe-25Cr-7Mo-0.8C alloy vs temperature. (c) Lattice misfit between ferrite and the χ phase.

hand, when the χ phase is establishing the main (110) reflection, ferrite loses some of its intensity. Taking all this into account, it can be concluded that the transfer of atoms between ferrite and the χ phase is mediated via $M_{23}C_6$ carbides.

The lattice parameter of ferrite increases with temperature, however, at ~600 °C, its value saturates (Fig. 3a). It is interesting to note that linear growth of ferrite's lattice parameter can be observed in two regions, i.e. between 200 and 400 °C and between 650 and 1050 °C. However, the progression of the lattice parameter in both regions significantly varies. In the first region (200–400 °C), the coefficient of thermal expansion (CTE) is reported to be $11.67 \times 10^{-6}C^{-1}$, while in the second region its value is significantly greater: $21.18 \times 10^{-6}C^{-1}$. The noticeable changes in crystal lattice growth behavior vs temperature are most likely related to the magnetic transformation of ferrite from ferromagnetic to paramagnetic that occurs in the range of 500 and 650 °C. Such a wide range of magnetic transformation temperatures can be expected for materials that exhibit clear intradendritic segregation, e.g. rapidly solidified hypoeutectic alloys [28]. Additionally, the effect of atomic transfer between nonequilibrium phases and the onset of the χ phase formation on changes in ferrite lattice parameter should be noted. It should be therefore concluded that changes in magnetic properties and chemical composition of ferrite are reflected in its phononic properties and consequently in CTE. Clear signs of χ phase formation can also be noticed in a strain dependence on temperature for ferrite (Fig. 3a). It is clear that stress is released, due to possible atomic diffusion during χ phase formation.

Fig. 3b shows the lattice parameter and volume fraction for the χ phase in the Fe-25Cr-7Mo-0.8C alloy vs temperature. It is visible that the lattice parameter progressively increases with temperature up to 950 °C. Deviations from the linearity of the lattice parameter growth are most likely related to changes in the chemical composition of the χ phase. During in situ neutron experiment maximum volume fraction, 15.3% of the χ phase was found at 800 °C which is in good agreement with thermodynamic simulations (Fig. 1, Table 2). Such observations also suggest that the kinetics of the χ phase formation is the fastest at around 800 °C. Above 950 °C, the χ phase lattice parameter decreases, caused by an advanced dissolution process. The CTE of the χ phase, estimated to be between 750 and 900 °C, is $13.75 \times 10^{-6}C^{-1}$ and is significantly lower in comparison to ferrite in the same temperature range. The CTE of the $M_{23}C_6$ carbide was not determined, due to relatively low intensity of its reflections. Nevertheless, according to Zhang and Komizo [36], who investigated heat-resistant steel, the CTE of the $M_{23}C_6$ carbide is around $9 \times 10^{-6}C^{-1}$ below 800 °C and $16 \times 10^{-6}C^{-1}$ above this temperature. The authors explained the distinct CTE change above 800 °C by coarsening and changes in the chemical composition of $M_{23}C_6$ carbides. In general, materials expand or contract as the temperature changes, therefore:

$$\varepsilon^T = \alpha(\Delta T) \tag{1}$$

Table 2
ThermoCalc predictions of the volume fraction (V_v) and chemical compositions of phases present in the Fe-25Cr-7Mo-0.8C alloy at 650, 800 and 1000 °C.

Phase	Temperature (°C)	V_v (%)	Atomic [%]			
			C	Cr	Mo	Fe
Ferrite	650	62	3.08E-04	16.12	0.60	Bal.
	800	68	8.82E-03	18.42	1.30	Bal.
	1000	83	0.13	20.48	3.21	Bal.
$M_{23}C_6$	650	16	20.69	61.15	9.72	Bal.
	800	16	20.69	58.13	8.77	Bal.
	1000	15	20.69	54.60	7.02	Bal.
χ phase	650	22	0	26.76	8.92	Bal.
	800	16	0	24.29	9.91	Bal.
	1000	2	0	22.88	12.54	Bal.

where ε^T is a thermal strain, α is the CTE and ΔT is the temperature change. If thermal-induced changes of dimensions are inhibited for some reason, then thermal-mechanical stresses can arise. In the case of the investigated Fe-25Cr-7Mo-0.8C alloy, changes in the dimensions of the strengthening phases (i.e. carbides and the χ phase) induced by thermal effects are counteracted by the surrounding ferritic matrix. Therefore, these strengthening phases together with the ferritic matrix would be expected to lead to residual stresses on cooling from formation temperature caused by mismatch of CTE. The greater the difference in CTE between phases the greater the thermal-mechanical stresses and local strain of the phases' crystal lattice. In terms of wear-resistant materials, local stresses (if they are tensile) can facilitate micro-crack propagation and spalling of strengthening phases [37].

The crystallographic relationship between ferrite and χ phase, observed in duplex stainless steels, has been suggested by Nilsson et al. [38] to be:

$$\langle 001\rangle_\chi // \langle 001\rangle_\alpha.$$

Based on neutron diffraction data, it was found that interplanar spacing of ferrite and χ phase follows $d_{(001)\ \text{ferrite}} \approx d_{(003)\ \chi\ \text{phase}}$, with misfit presented in Fig. 3c. The lattice misfit δ, can be calculated by following equation:

$$\delta = \frac{d_{(003)\ \chi\ \text{phase}} - d_{(001)\ \text{ferrite}}}{a_{(001)\ \text{ferrite}}} \tag{2}$$

where: $d_{(003)\ \chi\ \text{phase}}$ and $d_{(001)\ \text{ferrite}}$ are the interplanar spacing of the (003) χ phase and (001) ferrite, respectively. The lattice misfit is in the range of 3.58 and 3.82% and decreases with the increase in temperature. When the χ-phase is fully dissolved above 1050 °C (Figs. 2 and 3b), the lattice parameter of ferrite saturates again. This time, it seems to be connected to the vicinity of the solidus of the alloy (Fig. 1), which is confirmed by the sudden drop in the (110) ferrite reflection, presented in Fig. 2b.

3.2. Ex situ analysis of the alloy

3.2.1. Phase composition

Fig. 4 presents XRD results of the alloy in as-cast state and after heat treatment for 4 h at 650, 800 and 1000 °C. In as-cast state, the alloy contains ferrite and $M_{23}C_6$ carbides. This observation suggests TCP phase formation in the alloy is hampered during rapid cooling after solidification. After annealing at 650 °C, the formation of the χ phase was observed. Simultaneously, the blurring of carbide peaks and a decrease in their intensity in comparison to as-cast state was noted. Interestingly, according to thermodynamic simulations (Fig. 1), the precipitation of χ phase should not affect the volume fraction of $M_{23}C_6$ carbides, however, changes in their chemical composition can be expected. Predictions concerning the chemical composition of equilibrium phases at 650, 800 and 1000 °C are given in Table 2. It is visible that the equilibrium contents of elements in each phase clearly varies with temperature. The χ phase contains a high amount of chromium and molybdenum. In the case of the investigated alloy, the phase fractions and their chemical composition in the as-cast state of the rapidly solidified Fe-25Cr-7Mo-0.8C alloy is shifted from equilibrium state. Therefore, thermally-activated processes during alloy annealing, such as atomic diffusion and precipitation of the χ phase during annealing, cause significant changes in the chemical composition of ferrite and $M_{23}C_6$ carbides. Most probably, the blurring of $M_{23}C_6$ carbide peaks on the XRD pattern is related to the widened spectrum of their chemical composition and lattice parameters, especially in comparison to as-cast state, which is in agreement with the in situ experiment, discussed in Section 3.1. After annealing at 800 °C, ferrite, both $M_{23}C_6$ carbide and χ phase peaks are visible. Nevertheless, the position of the χ phase's peaks change in comparison to those after annealing at 650 °C, which suggests

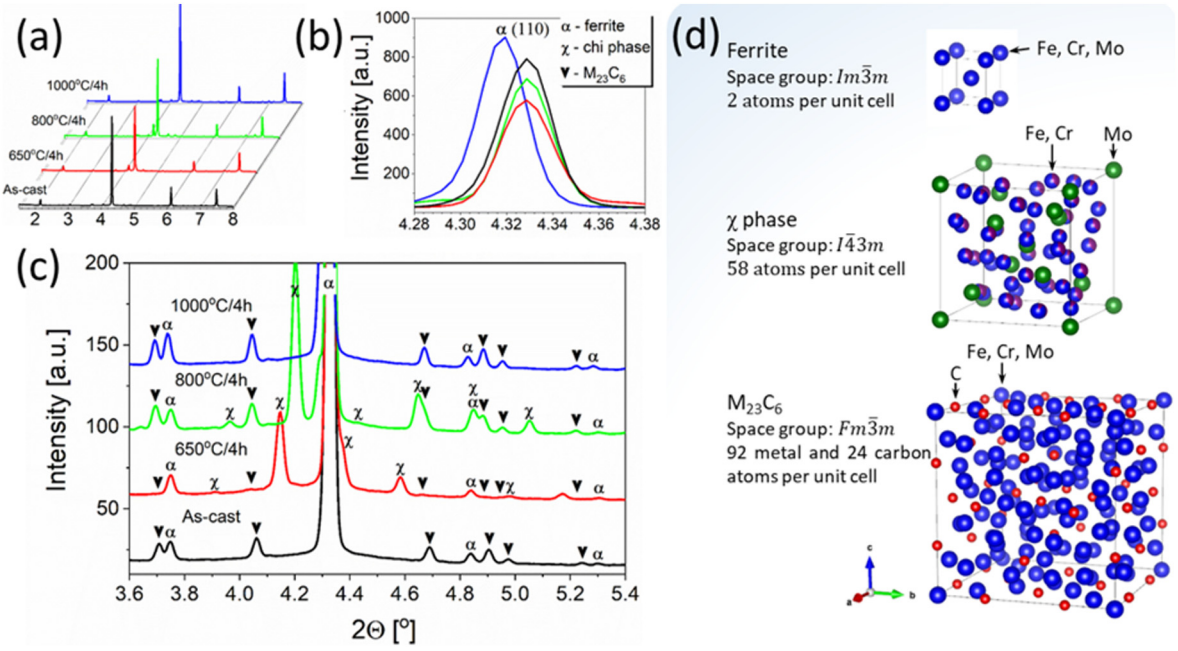

Fig. 4. (a) X-ray synchrotron diffraction patterns of the Fe-25Cr-7Mo-0.8C alloy in as-cast state and after heat treatment for 4 h at 650, 800 and 1000 °C. (b) Enlarged range of the (110) ferrite's reflection for different states. (c) Enlarged range of the strengthening phases' reflections group. (d) Unit cell models of phases, observed in the alloy, generated using the VESTA software [39].

changes in chemical composition, lattice parameters and, consequently, misfit with the ferritic matrix. The misfit between ferrite and χ phase is reported to be 4.39 and 3.01% for samples after annealing at 650 and 800 °C, respectively. Heat treatment at 1000 °C caused a shift in ferrite's peaks to lower values of 2Θ angle. This corresponds to an increase in ferrite lattice parameter values, which most probably is related to the

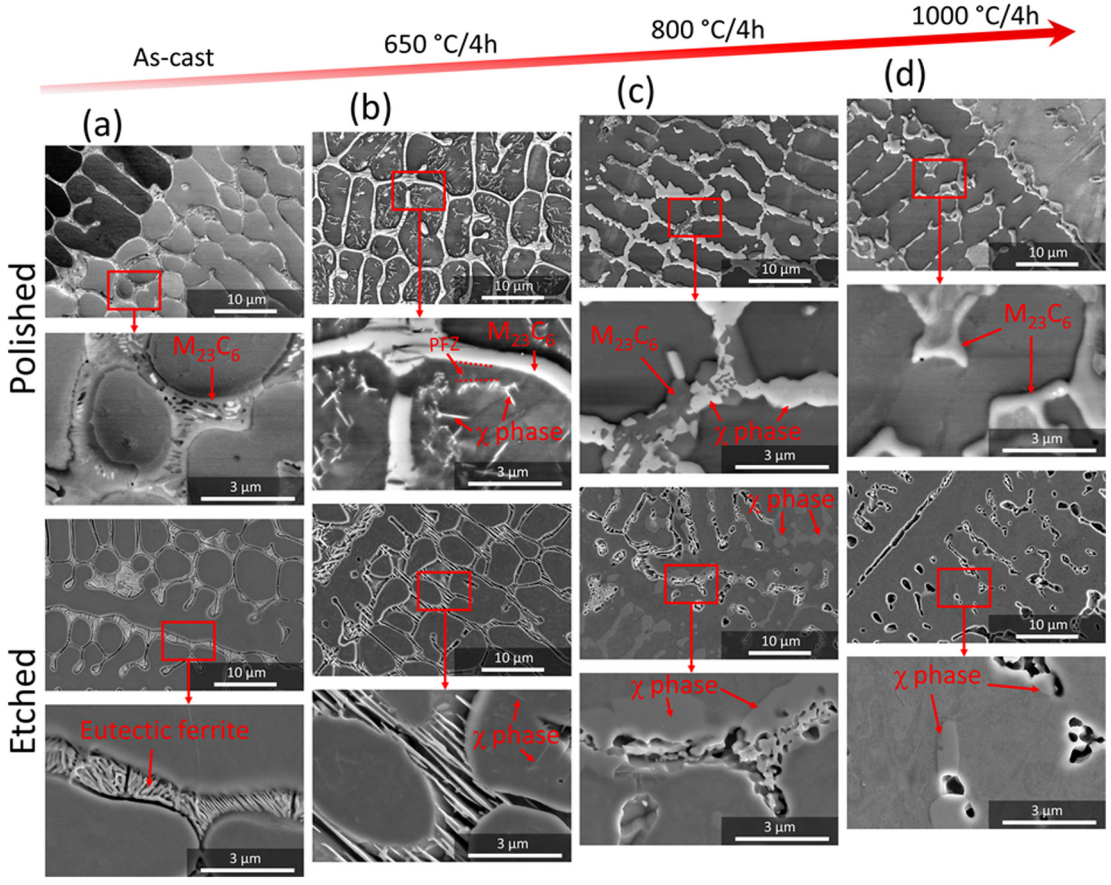

Fig. 5. Microstructure of the Fe-25Cr-7Mo-0.8C alloy in (a) as-cast state and after heat treatment for 4 h at (b) 650, (c) 800 and (d) 1000 °C. PFZ – precipitation-free zone. Polished samples – SEM-BSE, etched samples – SEM-SE.

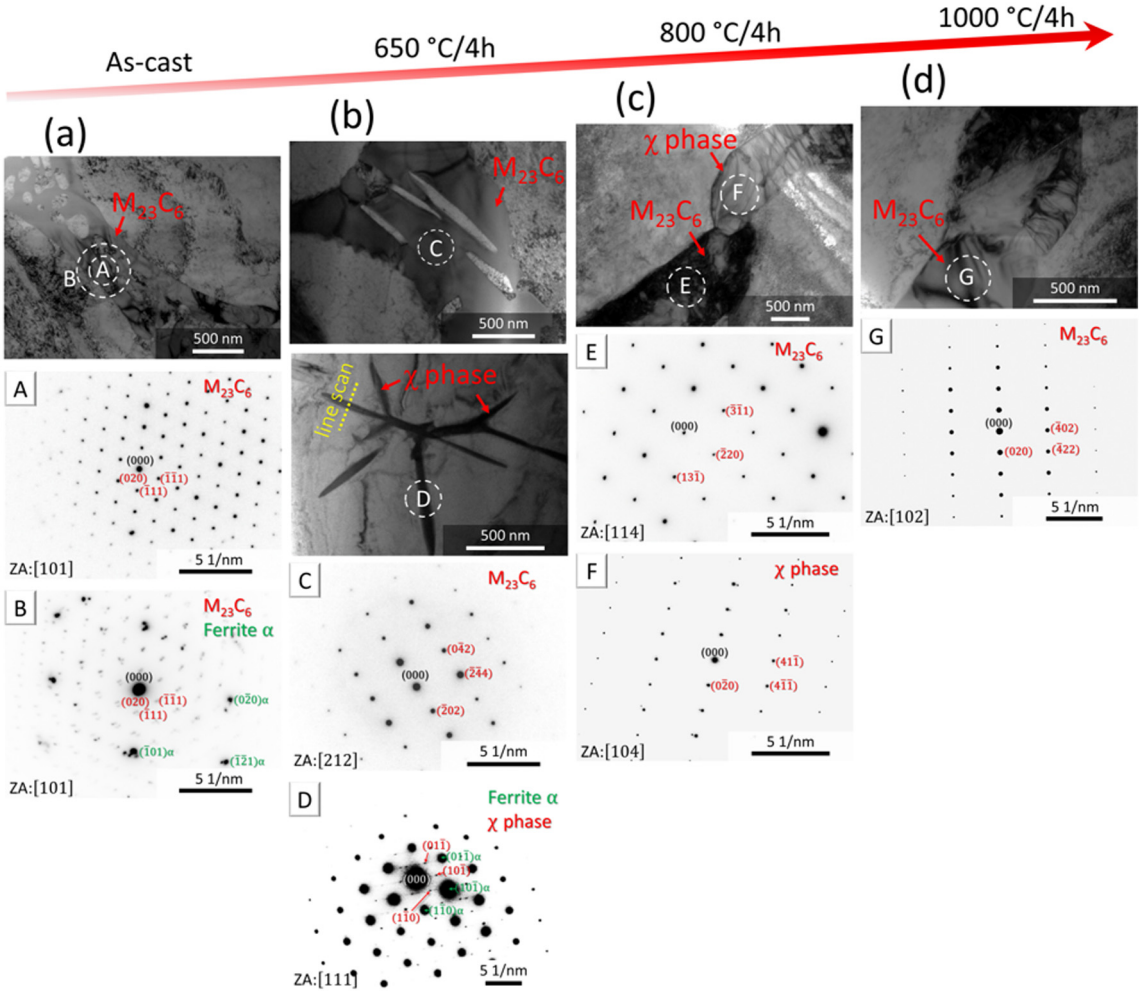

Fig. 6. Microstructure of the Fe-25Cr-7Mo-0.8C alloy in (a) as-cast state and after heat treatment for 4 h at (b) 650, (c) 800 and (d) 1000 °C revealed by TEM-BF and SAED.

enrichment of ferrite in chromium and molybdenum (Table 2), as they possess greater atomic diameters in comparison to iron [40]. According to the thermodynamic simulations (Fig. 1) at 1000 °C, approximately 2% of the alloy's volume fraction is expected to consist of the χ phase. However, no χ phase peaks were detected, suggesting either the absence of this phase or the amount being below the detection limit of the XRD technique. It is important to note that rapid cooling at the rate of 100 °C/s, after annealing at 1000 °C was fast enough to hamper the formation of a detectable amount of χ phase during the cooling process.

3.2.2. Microstructure evolution

Figs. 5 and 6 show the evolution of the microstructure after heat treatment. In as-cast state, the eutectic carbides of the $M_{23}C_6$ type have a morphology of interconnected plates that form a continuous network. The carbides in the outer region of the eutectic are clearly thicker in comparison to other carbides (Figs. 5a and 6a), which is associated to solid state nucleation and growth of secondary carbides on the primary carbide/ferrite interface [20,28]. The following orientation relationship was noted between ferrite and $M_{23}C_6$ type carbides (Fig. 6a):

$$\left(\bar{1}01\right)_{ferrite} // \left(\bar{1}11\right)_{M_{23}C_6}$$

which is consistent with the previously reported Kurdjumow-Sachs orientation relationship for these phases [41,42].

Annealing at 650 °C caused significant change in the morphology of the eutectic carbides in comparison to as-cast state. On polished samples, it seems that interdendritic regions exhibit a continuous form of $M_{23}C_6$ carbides (Fig. 5b), the presence of which was confirmed using selected area electron diffraction (SAED) (Fig. 6b). As the A2 solution dissolves $M_{23}C_6$ carbides, the plate-like morphology of the eutectic ferrite was revealed after electrolytic etching. The χ phase, which nucleated in dendrites with a morphology of interconnected needle-shaped precipitates, was also observed (Figs. 5b and 6b). The specific morphology of the χ phase is associated to its high misfit with the matrix (see Section 3.1). In principle, in the case of TCP phases, such as the χ

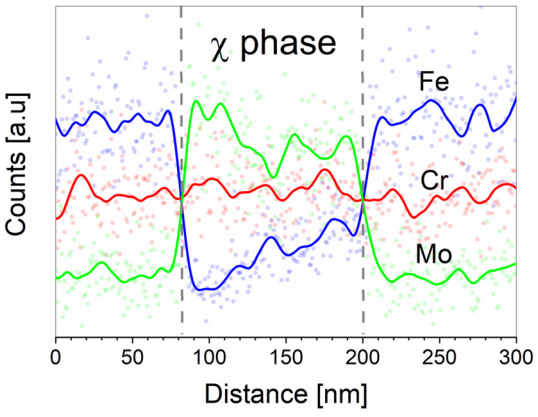

Fig. 7. STEM/EDX line scan across the χ phase precipitate, marked in Fig. 6b.

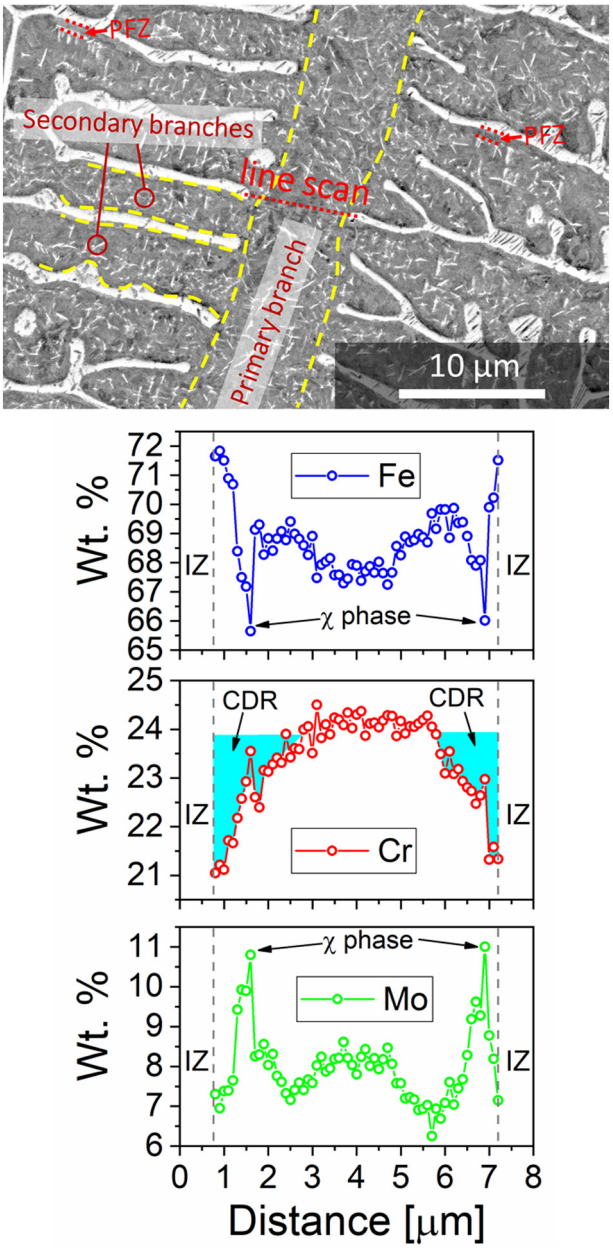

Fig. 8. SEM/EDX line scan across the primary branch of dendrites after annealing for 4 h at 650 °C. PFZ – precipitation-free zone, CDR - chromium depleted regions, IZ – interdendritic zone.

phase, specific morphologies, i.e. plate- or needle-like, are a consequence of a need to minimize the misfit energy of crystal lattices at the coherent boundaries between the precipitation and the matrix [43–46]. In other words, if the precipitate has a low misfit value with the matrix in only one direction, it will tend to exhibit needle-like morphology, due to the desire to minimize its size in the two other directions, where the misfit is large. In the situation when the precipitation has a low misfit in two non-parallel directions, it will increase in size and form a plate-like shape, defined by these two directions. Once again, the phase will aim to minimize the lattice strain energy in the third direction where there is a large misfit of crystal lattices. Furthermore, if different crystallographic relationships between the precipitate of one phase and the matrix are observed, then various lattice parameters within the precipitations can be expected [47].

Fig. 7 clearly demonstrates that the χ phase is enriched in molybdenum in comparison to the surrounding ferrite, which is in agreement with thermodynamic predictions (Table 2). However, no significant differences in chromium contents between the χ phase and ferrite were found. This suggests that the nucleation and growth of the χ phase is mainly controlled by the mobility of molybdenum atoms at 650 °C. Between the carbides in the interdendritic zone (IZ) and the χ phase within the dendrites, a precipitation-free zone (PFZ) is visible (Fig. 5b). The presence of the PFZ indicates the occurrence of depleted regions in alloying elements, i.e. chromium and possibly molybdenum, which are χ phase formers. Fig. 8 shows chemical distribution profiles, collected across the primary branch of dendrites after annealing for 4 h at 650 °C. It should be taken into account that experimental data can be slightly overestimated, especially in the vicinity of primary or secondary phases, due to a greater interaction volume between the electron beam and sample in comparison to the step size [28]. Nevertheless, chromium depleted regions (CDR) can be observed in the vicinity of carbides located in interdendritic zones. The presence of CDR is related with the precipitation of secondary carbides on the interface between primary carbides and the matrix [28,29]. Clear peaks, related to the χ phase, are visible on the chemical distribution profiles.

Fig. 9a presents a graphical illustration of the standard calculation method of the maximum chemical driving force for nucleation, i.e. in the absence of capillarity. If elastic strain is excluded, $\Delta G_m^{\alpha\to\beta}$ is the chemical driving force for nucleation. From Fig. 9a it is visible that the $\Delta G_m^{\alpha\to\beta}$can be determined by finding the vertical distance between the extrapolated tangent to G^{α} at X_B^{matrix} and G^{β} [48]. Fig. 9b shows the effect of chromium and molybdenum on the driving force for nucleation of the χ phase at 650 °C for the model Fe-xCr-xMo-0.8C alloy. Calculations were performed using ThermoCalc software and TCFE7 database. During the simulations, ferrite and the $M_{23}C_6$ carbide were selected as entered phases. The obtained results should be considered as an approximation of the general trends, as simulations were carried out for the modelled alloy, whereas the tested alloy has a slightly different

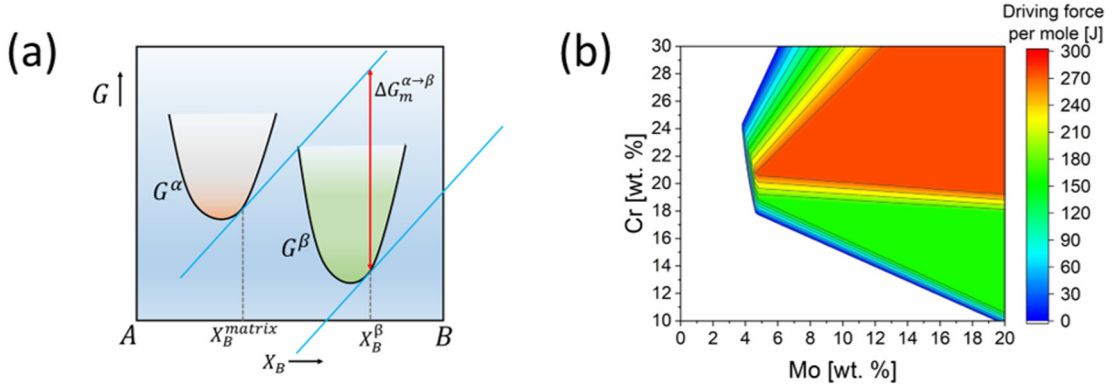

Fig. 9. (a) Graphical illustration of the chemical driving force for nucleation ($\Delta G_m^{\alpha\to\beta}$) standard calculation method, adapted from [48]. (b) Effect of chromium and molybdenum on the driving force for nucleation of the χ phase at 650 °C for the model Fe-xCr-xMo-0.8C alloy.

Table 3
Vickers hardness, nanoindentation hardness and indentation modulus of the Fe-25Cr-7Mo-0.8C alloy. The units are in GPa.

Load	9.8 N	1 mN	
	Vickers hardness	Nanoindentation hardness	Indentation modulus
As-cast	3.06 ± 0.03	4.84 ± 2.28	205 ± 19
650 °C/4 h	3.55 ± 0.05	5.30 ± 2.51	194 ± 18
800 °C/4 h	3.58 ± 0.04	6.32 ± 4.16	210 ± 24
1000 °C/4 h	2.73 ± 0.06	5.74 ± 3.28	230 ± 23

chemical composition. Additionally, in the case of the synthesized alloy, casting stresses and configuration of the matrix crystal lattice defects can also play some role in terms of nucleation of secondary phases. With increasing molybdenum contents, the driving force for nucleation of the χ phase successively increases. However, in the case of chromium, it initially increases to the field of maximum value of around 300 J, and then gradually decreases with the increase in chromium contents. Above approx. 12.2% of molybdenum contents, the chromium in the investigated range directly increases the driving force for nucleation. Therefore, it seems that the best conditions in terms of local chemical composition to overcome the nucleation barrier for the χ phase occur in some distance from the eutectic carbides located in the IZ. The evidence of the χ phase precipitation in some distance from the eutectic carbides is visible in the microstructure of the alloy in the form of PFZ (Figs. 5b and 8).

After annealing at 800 °C, the χ phase was observed in both dendrites and the IZ (Fig. 5c). Its presence was confirmed by XRD (Fig. 4) and SAED (Fig. 6c). In Fig. 5c, it can be observed that the χ phase nucleated on the carbide/matrix interface and grew at the expense of the eutectic ferrite and ferrite near the IZ. On the etched sample, it is visible that the distribution of the χ phase in the IZ is not uniform and regions with lower or greater volume fraction can be found. This phenomenon is most probably related to the micro-segregation of alloying elements during solidification. The chemical composition of the χ phase was determined using point EDX analysis. It contains approx. 29% of Cr and 11% of Mo (in at. % ± 1 at. %). The contents of chromium and molybdenum is slightly higher in comparison to thermodynamic predictions (Table 2). In the case of eutectic carbides, significant change in their morphology in comparison to as-cast state was observed. They form a continuous network and individual carbide plates are no longer visible.

Annealing at 1000 °C caused the coarsening of $M_{23}C_6$ carbides (Figs. 5 and 6). Consequently, the continuous network of carbides, observed in the previously described states, is interrupted. After etching, a small amount of the χ phase was also found, which is in agreement with thermodynamic predictions (Table 2).

3.2.3. Hardness analysis

The results of Vickers hardness, nanoindentation hardness and indentation modulus of the Fe-25Cr-7Mo-0.8C alloy in different states are summarized in Table 3. In as-cast state, the Vickers hardness of the alloy is 3.06 GPa. After heat treatment for 4 h at 650 and 800 °C, the Vickers hardness of the alloy increases to 3.55 and 3.58 GPa, respectively. The increase in hardness with respect to as-cast state is related to the precipitation of the χ phase, the evolution of carbide morphology and changes in the phases' chemical composition. A significant change in morphology of eutectic carbides and most probably reduction of casting stresses after heat treatment at 1000 °C, caused a Vickers hardness reduction to 2.73 GPa.

As the alloy contains up to three phases with different properties, it is clear that the local hardness is not uniform, visible in the nanoindentation hardness maps (Fig. 10). The regions with high hardness can be easily distinguished. The shape of these regions corresponds to the shape of the IZ, where eutectic carbides and the χ phase, in the case of samples after annealing at 650 and 800 °C, were observed. Relatively large, high hardness regions were formed after annealing at 800 °C

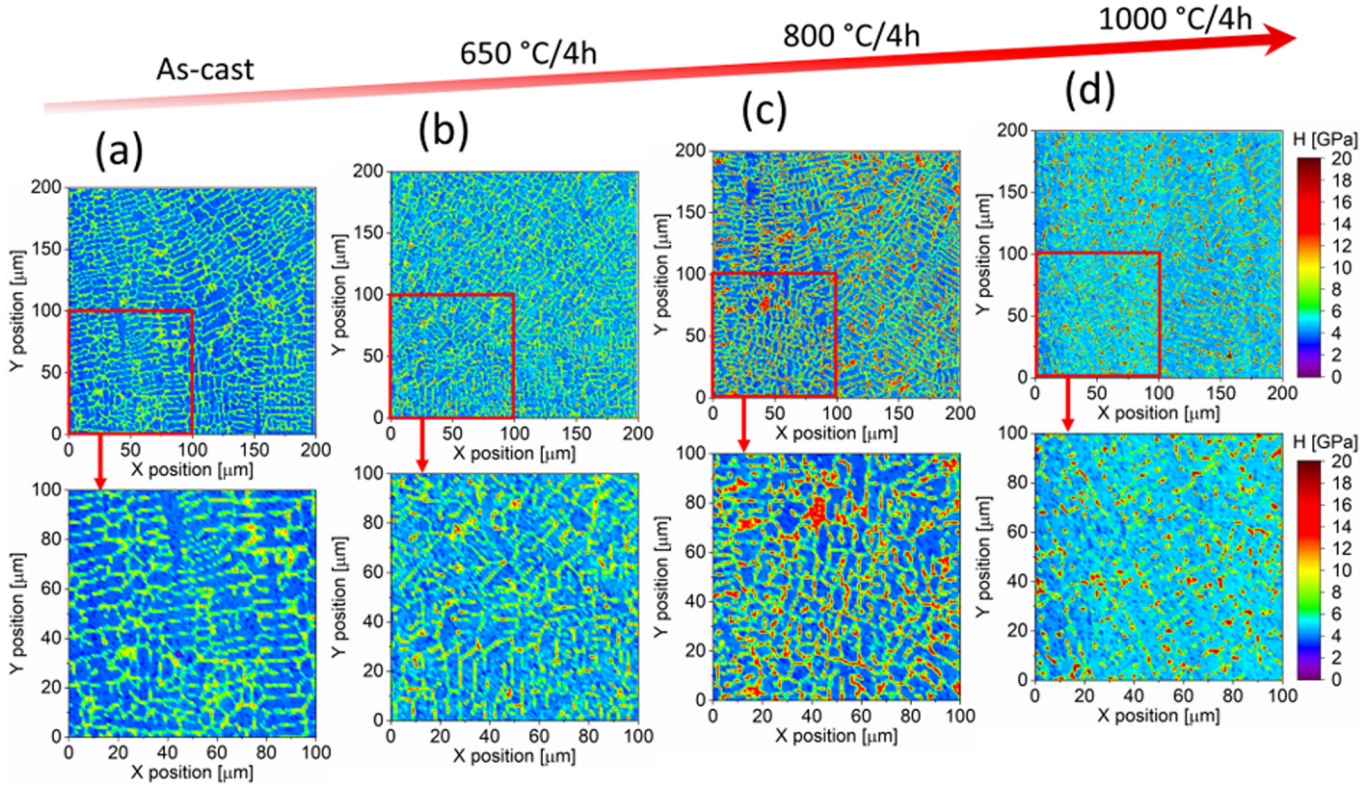

Fig. 10. Nanoindentation hardness maps performed with a 1 mN load on the Fe-25Cr-7Mo-0.8C alloy in (a) as-cast state and after heat treatment for 4 h at (b) 650, (c) 800 and (d) 1000 °C.

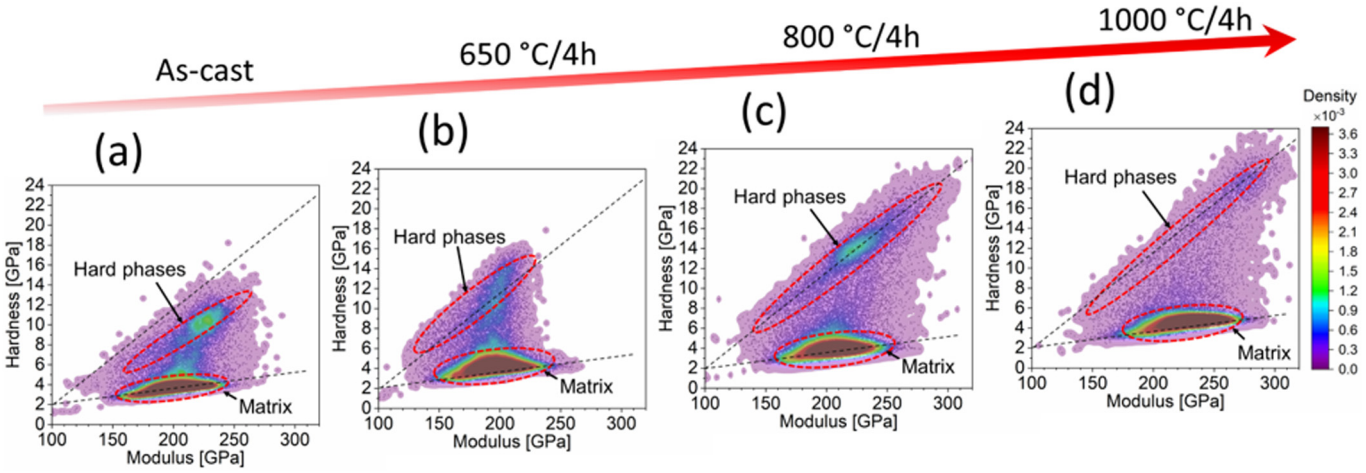

Fig. 11. 2D histogram maps of nanoindentation hardness vs indentation modulus of the Fe-25Cr-7Mo-0.8C alloy in (a) as-cast state and after heat treatment for 4 h at (b) 650, (c) 800 and (d) 1000 °C.

(Fig. 5c), due to the coarsening of the carbides and precipitation of the χ phase, visible in Fig. 10c. A similar situation can be observed after annealing at 1000 °C (Fig. 10d), however, in this case, hard "islands" are only related to the presence of coarsened carbides (Fig. 5d).

Fig. 11 shows 2D histogram contour plots of nanoindentation hardness as a function of indentation modulus with color density representation, performed using the kernel density estimation approach [49,50]. The regions in the graph corresponding to the matrix exhibit an elongated shape in the direction of the indentation modulus. Hardness points with high values correspond to regions containing hard phases (carbides and the χ phase). Between the "hard phases" and soft matrix, a transition region can be observed. In this region, the indentation plastic zone likely contained a composite of both hard and matrix phases. The hardness and indentation modulus histograms are presented in Fig. 12. It is clear that during measurements, most of the indents interacted with the ferritic matrix, as it is the dominating phase in terms of volume fraction in the alloy (Table 2, Fig. 5). Consequently, peaks corresponding to the matrix hardness are significantly higher in comparison to hard regions where carbides or the χ phase were found. However, the nanoindentation hardness distributions are not in agreement with Vickers hardness measurements, where the lowest hardness was noted for the state after annealing at 1000 °C. Nanoindentation hardness gives the lowest average value for the as-cast state (Table 3). Such differences are most probably related to the anisotropy of this property and localized characteristics of nanoindentation tests with very small loads (e.g. 1 mN) [51–53]. Furthermore, nanoindentation hardness values exceed Vickers hardness values due to the indentation size effect, which is commonly observed at small indentation depths (in this case, depths were between 50 and 150 nm) [54,55]. The full width at half maximum of the ferritic matrix hardness, observed in different states, is approx. 1 GPa. The relatively wide distribution of hardness is related to many overlapping factors, such as chemical inhomogeneity, presence of grain or subgrain boundaries, non-uniform dislocation density in the matrix, presence of secondary phases (e.g. the χ phase) and the effect of surrounding phases on the plastic zone.

From indentation modulus histograms (Fig. 12b), it is visible that their distribution for different states is similar except the histogram for the state after annealing at 1000 °C, which is shifted to higher values. Such an observation can be related to a change in chemical composition and properties of the phases after annealing (Table 2) and/or low statistics in terms of number of investigated grains. As the grain sizes in the investigated alloy are in the range from several dozen to several hundred μm and the investigated area was 200 × 200 μm, it can be concluded that only a few grains were analyzed. It is therefore possible that hardness maps for the analyzed states were performed on grains with different orientations and properties. That would explain the differences between macroscopic Vickers hardness and nanoindentation hardness trends and different indentation modulus values, especially after heat treatment at 1000 °C in comparison to other states.

Ferrite is an iron-based solid solution and exhibits a clear anisotropy of elastic properties [56]. However the elastic properties of $M_{23}C_6$ carbides are almost isotropic [57]. In Table 4, the elastic constants, calculated Young's modulus using the Voigt-Reuss-Hill [58–60]

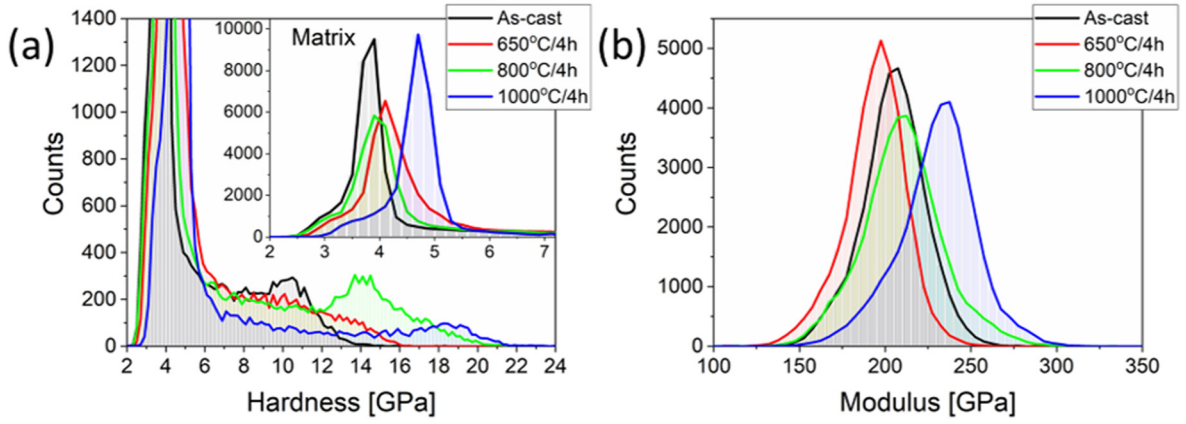

Fig. 12. Nanoindentation hardness (a) and indentation modulus (b) histograms of the Fe-25Cr-7Mo-0.8C alloy in as-cast state and after heat treatment for 4 h at 650, 800 and 1000 °C.

Table 4
Elastic constants taken from Ref. [56, 57], calculated Young's modulus E and Zener's (A) anisotropy factor of pure Fe and the $Cr_{23}C_6$ compound. The Zener's anisotropy factor was calculated using formula $A = 2C_{44} / C_{11} - C_{12}$ [61]. The units are in GPa.

Phase	C_{11}	C_{12}	C_{44}	E	$E_{\langle 100\rangle}$	$E_{\langle 110\rangle}$	$E_{\langle 111\rangle}$	A
Fe	233.1	135.4	117.8	213.2	133.6	222.7	286.4	2.41
$Cr_{23}C_6$	471.6	215.7	135.1	345.9	336.2	348.3	352.6	1.06

approximation and Zener's anisotropy factor (A) for pure iron and $Cr_{23}C_6$ compound in selected directions, are summarized. The Zener's anisotropy factor compares the (100)[001] and (110)[$\bar{1}$10] shear moduli [61]. The anisotropy of mechanical properties was also characterized by plotting Young's modulus vs crystallographic orientation in three-dimensional space using spherical coordinates (Fig. 13). The directional dependence of Young's modulus can be written as:

$$E\left(\vec{n}\right) = \frac{1}{S_{11} - (2S_{11} - 2S_{12} - S_{44})\left(n_1^2 n_2^2 + n_1^2 n_3^2 + n_2^2 n_3^2\right)} \quad (3)$$

where S_{ij} is the elastic compliance constant and n_1, n_2 and n_3 are the directional cosines. The projections of Young's modulus at (100) and (110) crystal planes were also plotted. The anisotropy of Young's modulus is clearly visible and is consistent with the calculated Zener's anisotropy factor. The major phases in the investigated alloy have a different chemical composition in comparison to pure iron and the $Cr_{23}C_6$ phase, which can affect their properties [57]. Nevertheless, the data presented in Table 4 and Fig. 13 provide a valuable insight into the anisotropy of these phases. The Young's modulus for pure iron exhibits clear anisotropy, reflected in a high value of the Zener's factor, i.e. 2.41. The Young's modulus for iron in the softest ⟨100⟩ directions is 133.6 GPa, while for the ⟨111⟩ hardest directions it is 286.4 GPa. In the case of the $Cr_{23}C_6$ compound, the Young's modulus anisotropy is much lower (1.06 Zener's anisotropy factor) and varies between 336.2 and 352.6 GPa for the softest and the hardest directions, respectively. Therefore, the orientation dependence of indentation modulus for the Fe-based matrix can be expected. Nevertheless, it is known that the anisotropy of the indentation modulus, determined using the nanoindentation method, is much lower than the theoretical one due to the complex redistribution of the stress/strain field in different directions, from which the mechanical response derives from [51,52]. Furthermore, the indentation modulus can also be affected by material behavior (e.g. piling up of the soft matrix) [62].

3.2.4. Scratch tests

Fig. 14 depicts an example morphology of a groove obtained after scratch testing and the relation between the average scratch depth for five scratches with error bands vs load of the Fe-25Cr-7Mo-0.8C alloy in as-cast state and after heat treatment for 4 h at 650, 800 and 1000 °C. The highest scratch depth was noted for as-cast state. Interestingly, after heat treatment, clear changes in scratch depth were found. A clear difference in average scratch depth between investigated states is visible above the load of 100 mN. The alloy after heat treatment at 650 °C has a comparable hardness to the state after heat treatment at 800 °C. The average scratch depth for states after heat treatment at 650 °C and 800 °C is lower for almost the entire load range when compared to as-cast state and state after heat treatment at 1000 °C with lower hardness. Such observations suggests a correlation between macroscopic hardness (Table 3) and scratch depth. With increasing temperature, the volume fraction and morphology of the χ phase changes

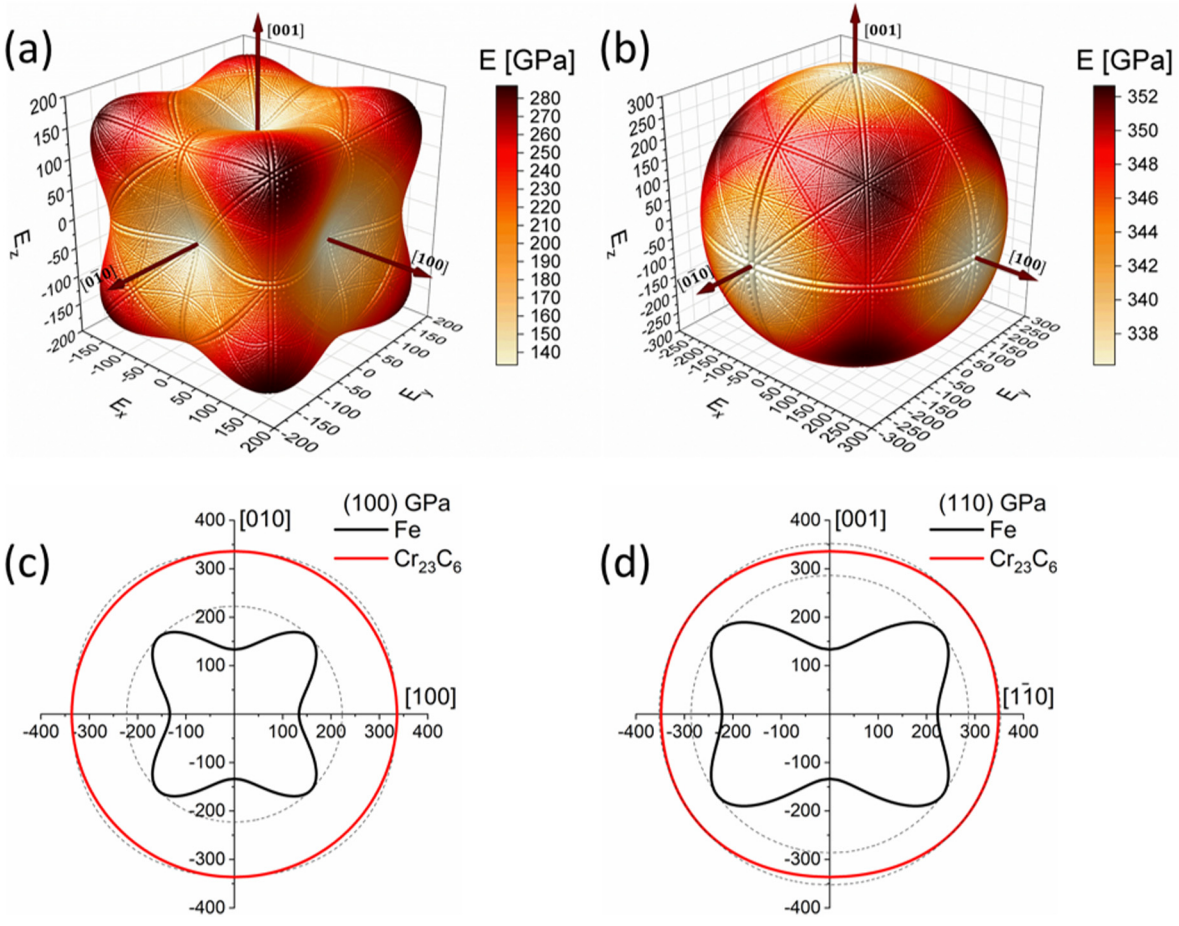

Fig. 13. The surface constructions of Young's modulus for (a) Fe and (b) $Cr_{23}C_6$ carbide and (c) (100) and (d) (110) planes projections of Young's modulus for these phases.

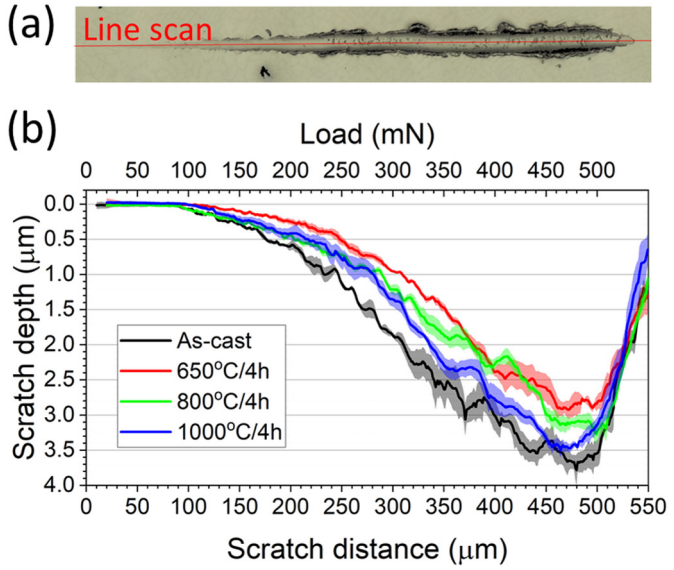

Fig. 14. (a) Example morphology of a groove obtained after scratch test using spheroconical diamond indenter of 10 μm radius with a marked red line along the scratch depth was measured. The groove was analyzed via confocal microscopy. (b) Average scratch depth for five scratches with error bands vs load of the Fe-25Cr-7Mo-0.8C alloy in as-cast state and after heat treatment for 4 h at 650, 800 and 1000 °C. (For interpretation of the references to color in this figure legend, the reader is referred to the web version of this article.)

(Figs. 1 and 5). Simultaneously, the morphology of the eutectic carbides also changes to form a continuous network of hard phases. In our previous work [63], it was found that the presence of a continuous, solid network of hard precipitations within interdendritic regions can lead to an increase in shear stress, necessary for their micro-cutting. In the case of states after heat treatment at 650 °C and 800 °C, the increase in hardness in comparison to as-cast state is mainly related to the precipitation of the χ phase and evolution of carbide morphology. These observations suggest that the volume fraction and morphology of the hard phases in the alloy plays the most important role in terms of wear resistance. However, it is very difficult to isolate the effect of the χ phase on this property. Undoubtedly, the presence of a high volume fraction of χ phase, formed after heat treatment at 650 °C and 800 °C on carbides/matrix interface and in dendrites, reduces the mean free path of the matrix and, consequently, can have a positive effect on scratch depth reduction.

Fig. 15 presents selected wear grooves after scratch tests of the Fe-25Cr-7Mo-0.8C alloy in as-cast state and after heat treatment for 4 h at 800 °C. It is visible that the matrix is plastically deformed and pushed to both sides of the groove via the micro-ploughing mechanism. In hard regions, i.e. containing carbides and/or the blocky χ phase, micro-cutting was the dominant wear mechanism. Such regions can be easily found due to the lack of plastically deformed material along the groove edges, which was marked in Fig. 15. In the case of the state after heat treatment at 800 °C, it is visible that the amount of material pushed to the groove's sides is lower in comparison to as-cast state. Furthermore, it seems that micro-chip formation is facilitated due to the presence of high volume fraction of hard phases. The presence of interfacial decohesion between matrix and carbides or χ phase is related to tensile stresses caused by tangential frictional forces, formed when the indenter slid over carbides [64,65]. The presented results suggest that microstructural evolution and increase in hard phases' volume fraction after heat treatment in the investigated alloy have a positive effect on the reduction of the average scratch depth. On the other hand, a higher volume fraction of hard phases facilitate the micro-chip formation and it changes the balance between main wear mechanisms from micro-ploughing to micro-cutting.

4. Conclusions

In the presented work, the Fe-25Cr-7Mo-0.8C alloy was synthesized using the suction-casting technique. It was designed to investigate the effect of the χ phase on the microstructure and properties of a rapidly solidified Fe-based hypoeutectic alloy. The alloy was studied in situ and ex situ in as-cast state and after heat treatment for 4 h at 650, 800 and 1000 °C. The following conclusions were formed:

1. Rapid cooling after solidification or heat treatment at 1000 °C suppresses the χ phase formation.
2. The χ phase at low temperatures (650 °C) nucleates mainly in dendrites and exhibits a needle-like morphology, which is related to high misfit energy of crystal lattices at the coherent boundaries between the precipitation and the matrix. A precipitation-free zone was observed between eutectic carbides and the χ phase. This zone

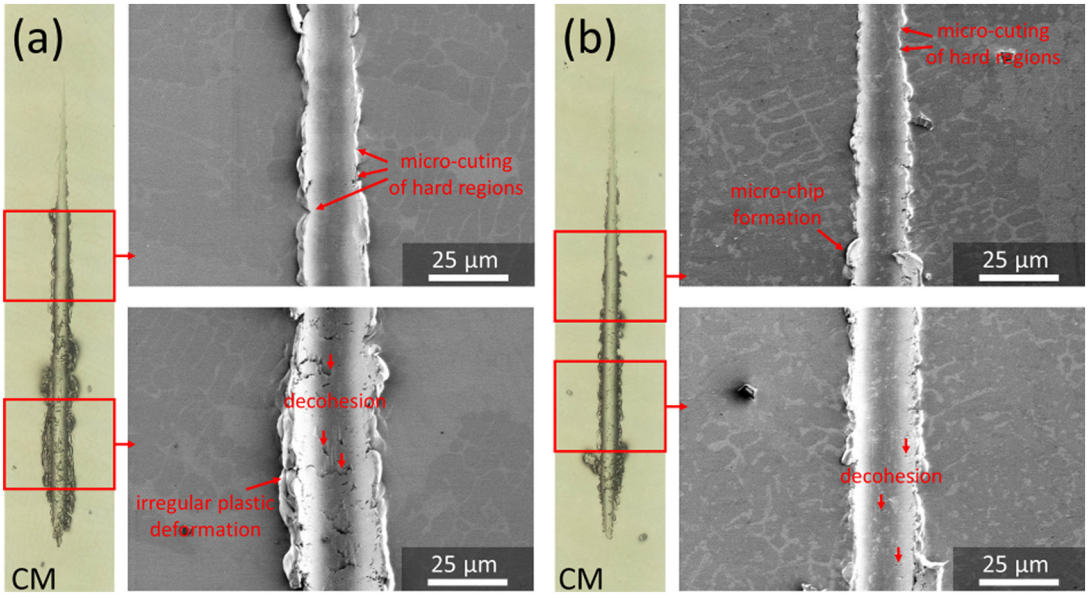

Fig. 15. Wear grooves after scratch tests of the Fe-25Cr-7Mo-0.8C alloy (a) in as-cast state and (b) after heat treatment for 4 h at 800 °C (b). CM – confocal microscope, other images SEM-SE.

overlaps with regions depleted in χ phase forming elements (mainly chromium), where a reduced χ phase driving force for nucleation can be found.
3. At higher temperatures (e.g. 800 °C), the χ phase nucleates on the carbide/matrix interface and grows at the expense of eutectic ferrite and ferrite near the interdendritic zone. The precipitations of the χ phase in dendrites have a blocky morphology. Simultaneously, with the precipitation of the χ phase, the eutectic carbides undergo a significant change in morphology to form a continuous and solid network of precipitates.
4. Heat treatment at temperatures (650 and 800 °C) at which a high volume fraction of χ phase precipitates was observed, induced an increase in hardness of about 16% in comparison to as-cast state. The formation of the χ phase on the carbides/matrix interface and within dendrites after heat treatment at 650 and 800 °C caused a clear reduction in the mean free path of the matrix. Simultaneously, the formation of the continuous, solid network of eutectic carbides was observed. Microstructural evolution of the alloy was reflected in the reduction of the average scratch depth.

Declaration of competing interests.

The authors declare that they have no known competing financial interests or personal relationships that could have appeared to influence the work reported in this paper.

CRediT authorship contribution statement

K. Wieczerzak: Conceptualization, Methodology, Validation, Formal analysis, Investigation, Resources, Writing - original draft, Writing - review & editing, Visualization, Project administration, Funding acquisition.**J. Michler:**Supervision, Resources.**J.M. Wheeler:**Investigation, Resources, Visualization.**S. Lech:**Investigation, Resources.**R. Chulist:** Investigation.**Ł. Gondek:**Investigation, Visualization.**J. Czub:**Investigation.**A. Hoser:**Investigation, Resources.**N. Schell:**Investigation, Resources.**P. Bała:**Supervision, Resources.

Acknowledgement

This work was supported by the Polish National Science Centre [grant number 2015/19/N/ST8/01157] (synthesis of the alloy, phase and microstructural analysis) and by the EMPAPOSTDOCS-II programme, that has received funding from the European Union's Horizon 2020 research and innovation programme under the Marie Skłodowska-Curie grant agreement number 754364 (nanoindentation experiments).

References

[1] L.E. Svensson, B. Gretoft, B. Ulander, H.K.D.H. Bhadeshia, Fe-Cr-C hardfacing alloys for high-temperature applications, J. Mater. Sci. 21 (1986) 1015–1019, https://doi.org/10.1007/BF01117388.
[2] D.G. Ahn, Hardfacing technologies for improvement of wear characteristics of hot working tools: a review, Int. J. Precis. Eng. Manuf. 14 (2013) 1271–1283, https://doi.org/10.1007/s12541-013-0174-z.
[3] H. Ocken, The galling wear resistance of new iron-base hardfacing alloys: a comparison with established cobalt- and nickel-base alloys, Surf. Coatings Technol. 76–77 (1995) 456–461, https://doi.org/10.1016/0257-8972(95)02573-1.
[4] D. Womersley, Hardfacing: not merely a reclamation process, Surf. Eng. 11 (1995) 43–46, https://doi.org/10.1179/sur.1995.11.1.43.
[5] P. Bala, J. Morgiel, G. Cios, K. Wieczerzak, T. Tokarski, Ni-Cr-Ta-Al-C complex phase alloy – design, microstructure and properties, Mater. Sci. Eng. A 711 (2018) 99–108, https://doi.org/10.1016/j.msea.2017.11.026.
[6] C. Sudha, P. Shankar, R.V.S. Rao, R. Thirumurugesan, M. Vijayalakshmi, B. Raj, Microchemical and microstructural studies in a PTA weld overlay of Ni-Cr-Si-B alloy on AISI 304L stainless steel, 202 (2008) 2103–2112, https://doi.org/10.1016/j.surfcoat.2007.08.063.
[7] B.K. Sreedhar, S.K. Albert, A.B. Pandit, Improving cavitation erosion resistance of austenitic stainless steel in liquid sodium by hardfacing - comparison of Ni and co based deposits, Wear 342–343 (2015) 92–99, https://doi.org/10.1016/j.wear.2015.08.009.
[8] K. Wieczerzak, M. Watroba, W. Bednarczyk, M. Madej, M. Marzec, T. Tokarski, P. Bala, The γ′-Ni_3(Al,Ta) phase triggered strengthening of the Ni-Ta-Al-Cr-C coating layer, deposited on austenitic stainless steel, Mater. Charact. 129 (2017) 367–377, https://doi.org/10.1016/j.matchar.2017.05.028.
[9] H. Gasan, F. Erturk, Effects of a destabilization heat treatment on the microstructure and abrasive wear behavior of high-chromium white cast iron investigated using different characterization techniques, Metall. Mater. Trans. A. 44 (2013) 4993–5005, https://doi.org/10.1007/s11661-013-1851-3.
[10] A. Wiengmoon, T. Chairuangsri, N. Chomsang, N. Poolthong, J.T.H. Pearce, Effects of heat treatment on hardness and dry wear properties of a semi-solid processed Fe-27 wt pct Cr-2.9 wt pct C cast iron, J. Mater. Sci. Technol. 24 (2008) 330–334.
[11] A.K. Bhaduri, R. Indira, S.K. Albert, B.P.S. Rao, S.C. Jain, S. Asokkumar, Selection of hardfacing material for components of the Indian prototype fast breeder reactor, J. Nucl. Mater. 334 (2004) 109–114, https://doi.org/10.1016/j.jnucmat.2004.05.005.
[12] K. Wieczerzak, P. Bała, Hypoeutectic Fe-Cr-Ni-Mo-C alloys additionally strengthened by the Frank-Kasper phases – design by means of the CALPHAD approach, Calphad 64 (2019) 248–257, https://doi.org/10.1016/j.calphad.2018.12.011.
[13] J.S. Kasper, The ordering of atoms in the chi-phase of the iron-chromium-molybdenum system, Acta Metall. 2 (1954) 456–461, https://doi.org/10.1016/0001-6160(54)90066-8.
[14] J.H. Westbrook, Temperature dependence of the hardness of secondary phases common in turbine bucket alloys, J. Met. 9 (1957) 898–904, https://doi.org/10.1007/BF03397938.
[15] B. Gwalani, A.V. Ayyagari, D. Choudhuri, T. Scharf, S. Mukherjee, M. Gibson, R. Banerjee, Microstructure and wear resistance of an intermetallic-based Al0.25Ti0.75CoCrFeNi high entropy alloy, Mater. Chem. Phys. (2017) 1–10, https://doi.org/10.1016/j.matchemphys.2017.06.034.
[16] C.P. Tabrett, I.R. Sare, M.R. Ghomashchi, Microstructure-property relationships in high chromium white iron alloys, Int. Mater. Rev. 41 (1996) 59–82, https://doi.org/10.1179/095066096790326075.
[17] R.D. Campbell, Ferritic stainless steel welding metallurgy, Key Eng. Mater. 69–70 (1992) 167–216, https://doi.org/10.4028/www.scientific.net/KEM.69-70.167.
[18] B. Weiss, R. Stickler, Phase instabilities during high temperature exposure of 316 austenitic stainless steel, Metall. Trans. 3 (1972) 851–866, https://doi.org/10.1007/BF02647659.
[19] M.J. Cieslak, A.M. Ritter, W.F. Savage, Chi-phase formation during solidification and cooling of CF-8M weld metal, Weld. J. 63 (1984) 133.
[20] K. Wieczerzak, P. Bala, M. Stepien, G. Cios, T. Koziel, Formation of eutectic carbides in Fe-Cr-Mo-C alloy during non-equilibrium crystallization, Mater. Des. 94 (2016) 61–68, https://doi.org/10.1016/j.matdes.2016.01.028.
[21] C.-M. Chang, C.-C. Hsieh, C.-M. Lin, J.-H. Chen, C.-M. Fan, W. Wu, Effect of carbon content on microstructure and corrosion behavior of hypereutectic Fe–Cr–C claddings, Mater. Chem. Phys. 123 (2010) 241–246, https://doi.org/10.1016/j.matchemphys.2010.04.003.
[22] A. Wiengmoon, J.T.H. Pearce, T. Chairuangsri, Relationship between microstructure, hardness and corrosion resistance in 20 wt.%Cr, 27 wt.%Cr and 36 wt.%Cr high chromium cast irons, Mater. Chem. Phys. 125 (2011) 739–748, https://doi.org/10.1016/j.matchemphys.2010.09.064.
[23] M. Pohl, O. Storz, T. Glogowski, Effect of intermetallic precipitations on the properties of duplex stainless steel, Mater. Charact. 58 (2007) 65–71, https://doi.org/10.1016/j.matchar.2006.03.015.
[24] T.H. Chen, K.L. Weng, J.R. Yang, The effect of high-temperature exposure on the microstructural stability and toughness property in a 2205 duplex stainless steel, Mater. Sci. Eng. A 338 (2002) 259–270, https://doi.org/10.1016/S0921-5093(02)00093-X.
[25] G. Fargas, M. Anglada, A. Mateo, Effect of the annealing temperature on the mechanical properties, formability and corrosion resistance of hot-rolled duplex stainless steel, J. Mater. Process. Technol. 209 (2009) 1770–1782, https://doi.org/10.1016/j.jmatprotec.2008.04.026.
[26] K.W. Chan, S.C. Tjong, Effect of secondary phase precipitation on the corrosion behavior of duplex stainless steels, Materials (Basel) 7 (2014) 5268–5304, https://doi.org/10.3390/ma7075268.
[27] B.V. Cockeram, Fracture toughness testing and toughening mechanisms of some commercial cobalt-free hardfacing alloys, Surf. Coatings Technol. 108–109 (1998) 377–384, https://doi.org/10.1016/S0257-8972(98)00600-8.
[28] K. Wieczerzak, A. Żywczak, J. Kanak, P. Bała, Magnetic detection of chromium depleted regions in metastable Fe-Cr-C alloy, Mater. Charact. 132 (2017) 293–302, https://doi.org/10.1016/j.matchar.2017.08.030.
[29] K. Wieczerzak, P. Bala, R. Dziurka, T. Tokarski, G. Cios, T. Koziel, L. Gondek, The effect of temperature on the evolution of eutectic carbides and $M_7C_3 \rightarrow M_{23}C_6$ carbides reaction in the rapidly solidified Fe-Cr-C alloy, J. Alloys Compd. 698 (2017) 673–684, https://doi.org/10.1016/j.jallcom.2016.12.252.
[30] J.O. Andersson, T. Helander, L. Höglund, P.F. Shi, B. Sundman, Thermo-Calc and DICTRA, computational tools for materials science, Calphad 26 (2002) 273–312, https://doi.org/10.1016/S0364-5916(02)00037-8.
[31] R. Chulist, L. Straka, A. Sozinov, T. Lippmann, W. Skrotzki, Modulation reorientation in 10M Ni-Mn-Ga martensite, Scr. Mater. 68 (2013) 671–674, https://doi.org/10.1016/j.scriptamat.2013.01.024.
[32] A.A. Coelho, TOPAS: General Profile and Structure Analysis Software for Powder Diffraction Data, Bruker AXS GmbH, Karlsruhe, Germany, 2003.
[33] H.M. Rietveld, A profile refinement method for nuclear and magnetic structures, J. Appl. Crystallogr. 2 (1969) 65–71, https://doi.org/10.1107/S0021889869006558.
[34] P.S. Phani, W.C. Oliver, A critical assessment of the effect of indentation spacing on the measurement of hardness and modulus using instrumented indentation testing, Mater. Des. 164 (2019), 107563. https://doi.org/10.1016/j.matdes.2018.107563.

[35] K.H. Zum Gahr, Wear by hard particles, Tribol. Int. 31 (1998) 587–596, https://doi.org/10.1016/S0301-679X(98)00079-6.
[36] X.F.F. Zhang, Y. Komizo, Direct observation of thermal stability of $M_{23}C_6$ carbides during reheating using in situ synchrotron X-ray diffraction, Philos. Mag. Lett. 93 (2013) 9–17, https://doi.org/10.1080/09500839.2012.728296.
[37] D. Galusek, R. Brydson, P.C. Twigg, F.L. Riley, Wet erosive wear of alumina densified with magnesium silicate additions, J. Am. Ceram. Soc. 76 (2001) 1767–1776, https://doi.org/10.1111/j.1151-2916.2001.tb00913.x.
[38] J.-O. Nilsson, T. Huhtala, P. Jonsson, L. Karlsson, A. Wilson, Structural stability of super duplex stainless weld metals and its dependence on tungsten and copper, Metall. Mater. Trans. A. 27 (1996) 2196–2208, https://doi.org/10.1007/BF02651874.
[39] K. Momma, F. Izumi, VESTA 3 for three-dimensional visualization of crystal, volumetric and morphology data, J. Appl. Crystallogr. 44 (2011) 1272–1276, https://doi.org/10.1107/S0021889811038970.
[40] C. Kittel, Introduction to Solid State Physics, Eight ed. John Wiley & Sons, 2005.
[41] K.H. Kuo, C.L. Jia, Crystallography of $M_{23}C_6$ and M_6C precipitated in a low alloy steel, Acta Metall. 33 (1985) 991–996, https://doi.org/10.1016/0001-6160(85)90193-2.
[42] P.R. Howell, J.V. Bee, R.W.K. Honeycombe, The crystallography of the austenite-ferrite/carbide transformation in Fe-Cr-C alloys, Metall. Trans. A. 10A (1979) 1213–1222, https://doi.org/10.1007/BF02811976.
[43] C.M.F. Rae, M.S.A. Karunaratne, C.J. Small, R.W. Broomfield, C.N. Jones, R.C. Reed, Topologically close packed phases in an experimental rhenium-containing single crystal superalloy, Superalloys (2000) 767–776, https://doi.org/10.7449/2000/Superalloys_2000_767_776.
[44] Q.Z. Chen, N. Jones, D.M. Knowles, The microstructures of base/modified RR2072 SX superalloys and their effects on creep properties at elevated temperatures, Acta Mater. 50 (2002) 1095–1112, https://doi.org/10.1016/S1359-6454(01)00410-4.
[45] R.A. Hobbs, L. Zhang, C.M.F. Rae, S. Tin, Mechanisms of topologically close-packed phase suppression in an experimental ruthenium-bearing single-crystal nickel-base superalloy at 1100 °C, Metall. Mater. Trans. A Phys. Metall. Mater. Sci. 39 A (2008) 1014–1025, https://doi.org/10.1007/s11661-008-9490-9.
[46] S. Gao, Z.Q. Liu, C.F. Li, Y. Zhou, T. Jin, In situ TEM investigation on the precipitation behavior of μ phase in Ni-base single crystal superalloys, Acta Mater. 110 (2016) 268–275, https://doi.org/10.1016/j.actamat.2016.03.046.
[47] H. Long, Y. Liu, S. Mao, H. Wei, J. Zhang, S. Ma, Q. Deng, Y. Chen, Z. Zhang, X. Han, Minimum interface misfit criterion for the precipitation morphologies of TCP phases in a Ni-based single crystal superalloy, Intermetallics 94 (2018) 55–64, https://doi.org/10.1016/j.intermet.2017.12.020.
[48] K.C. Russell, Nucleation in solids: the induction and steady state effects, Adv. Colloid Interf. Sci. 13 (1980) 205–318, https://doi.org/10.1016/0001-8686(80)80003-0.
[49] M. Rosenblatt, Remarks on some nonparametric estimates of a density function, Ann. Math. Stat. 27 (1956) 832–837, https://doi.org/10.1214/aoms/1177728190.
[50] E. Parzen, On estimation of a probability density function and mode, Ann. Math. Stat. 33 (1962) 1065–1076, https://doi.org/10.1214/aoms/1177704472.
[51] J.J. Vlassak, W.D. Nix, Measuring the elastic properties of anisotropic materials by means of indentation experiments, J. Mech. Phys. Solids. 42 (1994) 1223–1245.
[52] P. Hausild, A. Materna, J. Nohava, Characterization of anisotropy in hardness and indentation modulus by nanoindentation, Met. Microstruct. Anal. 3 (2014) 5–10, https://doi.org/10.1007/s13632-013-0110-8.
[53] C.A. Brookes, J.B. O'Neill, B.A.W. Redfern, Anisotropy in the hardness of single crystals, Proc. Roy. Soc. Lond. A. 88 (1971) 73–88, https://doi.org/10.1098/rspa.1971.0055.
[54] K.W. McElhaney, J.J. Vlassak, W.D. Nix, Determination of indenter tip geometry and indentation contact area for depth-sensing indentation experiments, J. Mater. Res. 13 (1998) 1300–1306, https://doi.org/10.1557/JMR.1998.0185.
[55] M.F. Doerner, W.D. Nix, A method for interpreting the data from depth-sensing indentation instruments, J. Mater. Res. 1 (1986) 601–609.
[56] H.M. Ledbetter, R.P. Reed, Elastic properties of metals and alloys, I. iron, nickel, and iron-nickel alloys, J. Phys. Chem. Ref. Data 2 (1973) 531–617, https://doi.org/10.1063/1.3253127.
[57] Y. Liu, Y. Jiang, J. Xing, R. Zhou, J. Feng, Mechanical properties and electronic structures of $M_{23}C_6$ (M = Fe, Cr, Mn)-type multicomponent carbides, J. Alloys Compd. 648 (2015) 874–880, https://doi.org/10.1016/j.jallcom.2015.07.048.
[58] A. Reuss, Berechnung der Fliessgrenze von mischkristallen auf grund der blastizitatsbedingung fur einknstalle, Z. Angew. Math. Mech. 9 (1929) 49–58.
[59] W. Voigt, Lehrbuch der Kristallphysik, B.G. Teulne, Leipzig, 1928.
[60] R. Hill, The elastic behaviour of a crystalline aggregate, Proc. Phys. Soc. A. 65 (1952) 349–354.
[61] C.N. Reid, Deformation Geometry for Materials Science, 1st ed. Pergamon Press, Oxford, 1973.
[62] A.C. Fischer-Cripps, Nanoindentation, 3rd ed. Springer, New York, 2011.
[63] K. Wieczerzak, K. Pajor, K. Górecki, R. Chulist, P. Bała, Microstructural response on nickel addition in rapidly solidified ~Fe-25Cr-xNi-5Mo-0.8C [x = 0, 6, 11, 15, 21 wt. %] hardfacing alloys, J. Alloys Compd. 787 (2019) 186–195, https://doi.org/10.1016/j.jallcom.2019.02.110.
[64] H. Kong, M.F. Ashby, Wear mechanisms in brittle solids, Acta Metall. Mater. 40 (1992) 2907–2920, https://doi.org/10.1016/0956-7151(92)90455-N.
[65] Ö.N. Doğan, J.A. Hawk, Effect of carbide orientation on abrasion of high Cr white cast iron, Wear 189 (1995) 136–142, https://doi.org/10.1016/0043-1648(95)06682-9.